The Atom-Cavity Microscope: Single Atoms Bound in Orbit by Single Photons

C. J. Hood,[1] T. W. Lynn,[1] A. C. Doherty,[2] A. S. Parkins,[2]
H. J. Kimble[1]*

The motion of individual cesium atoms trapped inside an optical resonator is revealed with the atom-cavity microscope (ACM). A single atom moving within the resonator generates large variations in the transmission of a weak probe laser, which are recorded in real time. An inversion algorithm then allows individual atom trajectories to be reconstructed from the record of cavity transmission and reveals single atoms bound in orbit by the mechanical forces associated with single photons. In these initial experiments, the ACM yields 2-micrometer spatial resolution in a 10-microsecond time interval. Over the duration of the observation, the sensitivity is near the standard quantum limit for sensing the motion of a cesium atom.

We report a type of measurement capability that achieves continuous position measurement by using an optical cavity to enhance the sensitivity for atomic detection while achieving high spatial resolution. In this case, the signal-to-noise (S/N) ratio R_c for atomic detection within the cavity becomes $R_c \sim R_0 \sqrt{F}$, where R_0 is the S/N ratio for sensing the presence of the atom with absorption cross section σ within the resolution area A, $R_0 \sim \sqrt{\sigma \Delta t / A \tau}$ (Δt is the measurement time and τ is the minimum allowed interval between successive absorption events) (1, 2), and F is the cavity finesse (roughly the number of intracavity photon round trips during the cavity decay time) (3, 4). With low-loss dielectric coatings deposited on superpolished substrates, the cavity finesse F can be quite large, with the record value for a Fabry-Perot cavity being $F = 1.9 \times 10^6$ (5), thereby suggesting potentially large gains in sensitivity for sensing motion within the cavity (6).

Improving sensitivity by placing a sample inside a high-quality optical cavity is in and of itself a well-known technique, with implementations ranging from multipass absorption cells to high-finesse optical cavities (7–9). However, these experiments most often involve a concomitant loss in spatial resolution [with (resolution $\delta r = \sqrt{A}$) $\sim$ (cavity waist w_0) $\gg$ (wavelength λ)] and have usually detected changes of cavity transmission caused by ensembles of atoms or molecules.

In contrast, real-time modifications in cavity transmission wrought by single atoms within an optical cavity have been observed within the setting of cavity quantum electrodynamics (cavity QED), beginning in 1996 (10) and in several subsequent experiments (11–15). In fact, cavity transmission modified by a factor of 10^2 associated with the 80-μs passage of a single atom through a Fabry-Perot cavity was reported in (11). To translate this high sensitivity for atomic detection into a capability for atomic microscopy requires achieving $\delta r < w_0$ for motion within the cavity, attainable by trading back a fraction of the gain associated with large F for increased spatial resolution.

Toward this end, consider a cavity of length l driven by an input probe laser, with the transmitted light detected to generate a photocurrent, as shown in Fig. 1. The intracavity field $\vec{E}(\vec{r}')$ is $E_0\psi(\vec{r}')\vec{\epsilon}$, with cavity polarization vector $\vec{\epsilon}$ and spatially varying mode function $\psi(\vec{r}') = \cos(2\pi x/\lambda)\exp[-(y^2 + z^2)/w_0^2]$ for $-(l/2) < x < l/2$. An atom falling into the cavity modifies E_0; examples of the resulting variation are displayed in Fig. 2 for $\bar{m} \equiv |E_0|^2 \lesssim 1$ photon mean field strength. Because the large changes in $\bar{m}(t)$ evident in Fig. 2 are caused by the motion $\vec{r}(t)$ of a single atom within the cavity

mode, spatial resolution $\delta r < w_0$ can be achieved if the association between $\bar{m}(t)$ and $\vec{r}(t)$ can be quantified.

In fact, the quantum master equation (16) describing the radiative interaction between atom and cavity field allows E_0 to be calculated for any atomic position. Knowledge of E_0 in turn enables deduction of the total field transmitted by the cavity and thence of the photocurrent generated by measuring this transmitted field. We developed an algorithm that inverts this chain of deduction—namely, we infer the position $\vec{r}$ of a single atom within the cavity mode from the recorded photocurrent, albeit with some caveats. We can then use the cavity field as a microscope to track atomic motion in real time, with spatial resolution $\delta r \simeq 2$ μm attained in time $\delta t \simeq 10$ μs. These capabilities realize a form of time-resolved microscopy—the atom-cavity microscope (ACM).

Cavity quantum electrodynamics. Our work was carried out within the setting of cavity QED for which a single atom is strongly coupled to the electromagnetic field of a high-finesse (optical or microwave) cavity (16, 17). Here, the interaction energy between atom and cavity field is given by $\hbar g(\vec{r})$, where $g(\vec{r}) = g_0\psi(\vec{r})$ and $\hbar$ is Planck's constant divided by 2π. In a regime of strong coupling, the rate g_0 that characterizes the interaction of an atom with the cavity field for a single photon can dominate the dissipative rates for atomic spontaneous emission γ and cavity decay κ. Explicitly, $2g_0$ is the Rabi frequency for the oscillatory exchange of a single quantum between atom and cavity field, with $g_0\tau_0 = (V_0/V_C)^{1/2}$, where $\tau_0 = 1/2\gamma$ is the atomic lifetime, V_C is the cavity mode volume $V_C = (\pi/4)w_0^2 l$, and V_0 is the "radiative" volume $V_0 = \sigma c\tau_0$ (where c is the speed of light). For strong coupling ($g_0 \gg \kappa, \gamma$), the number of photons required to saturate an intracavity atom $n_0 \sim \gamma^2/g_0^2 \ll 1$ and the number of atoms required to have an appreciable effect on the intracavity field $N_0 \sim \kappa\gamma/g_0^2 \ll 1$, thereby enabling the observations of Fig. 2.

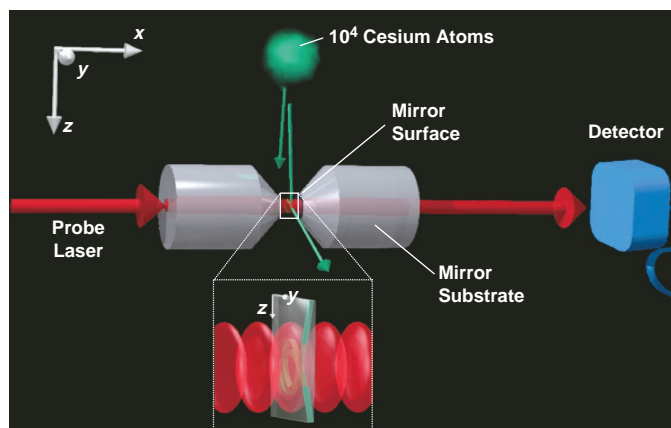These observations should be viewed within the context of important laboratory advances

[1]Norman Bridge Laboratory of Physics 12-33, California Institute of Technology, Pasadena, CA 91125, USA. [2]Physics Department, The University of Auckland, Private Bag 92019, Auckland, New Zealand.

*To whom correspondence should be addressed. E-mail: hjkimble@cco.caltech.edu

Fig. 1. Experimental schematic. Cesium atoms are captured in a magneto-optical trap (MOT) and dropped through a high-finesse optical cavity. A single atom (green arrow) transiting the cavity mode substantially alters the measured transmission of a probe beam through the cavity.

1447

that demonstrate the effect of strong coupling on the internal degrees of freedom of an atomic dipole coupled to the quantized cavity field, including the realization of diverse new phenomena such as the creation of nonclassical states of the radiation field (*18–20*). However, until now, the consequences of strong coupling for the external, atomic center-of-mass (CM) motion with kinetic energy E_k have remained largely unexplored experimentally (*11, 12, 14*). The seminal work of (*21, 22*) and numerous analyses since then (*23–27*) have made it clear that a rich set of phenomena should arise from the interaction of the mechanical motion of atoms with a quantized light field. In the regime of strong coupling for both the internal and external degrees of freedom, $g_0 \gg (E_k/\hbar, \gamma, \kappa)$, a single quantum is sufficient to profoundly alter the atomic CM motion, as shown, for example, in (*27*).

Following this theme, our experiment represents the observation of a single atom trapped by an intracavity field with $\bar{m} \simeq 1$ photon mean field strength. Such trapping is possible because the coherent coupling energy $\hbar g_0 \simeq 5.3$ mK is larger than the atomic kinetic energy $E_k \simeq 0.46$ mK for the cold atoms that fall into the cavity (Fig. 1).

Moreover, beyond providing single-quantum forces sufficient to trap atoms, strong coupling also enables real-time detection by way of the light emerging from the cavity (*10–15*), although actual atomic trajectories have not

been previously extracted. Stated more quantitatively, the ability to sense atomic motion within an optical cavity by way of the transmitted field can be characterized by the optical information $I = \alpha(g_0^2 \Delta t/\kappa) \sim \alpha R_c^2$, which roughly speaking is the number of photons collected as signal in time Δt with efficiency α as an atom transits between a region of optimal coupling g_0 and one with $g(\vec{r}) \ll g_0$. When $I \simeq 3 \times 10^4$ for $\Delta t = 30$ μs as in Fig. 2, atomic motion through the spatially varying cavity mode leads to variations in the transmitted field that can be recorded with high S/N ratio.

Atom trapping at the single-photon level. Relative to earlier work in cavity QED with cold atoms, we demonstrate a mechanism for trapping an atom within the cavity (*12*), rather than settling for a single transit through the mode waist (*10, 11, 13–15*). However, we emphasize at the outset that the operation of the ACM is not restricted to this particular trapping mechanism. The functions of trapping and sensing within the cavity mode can be separated, both in theory and in practice, as, for example, by way of the dipole-force trap of (*15*).

The conceptual basis for our scheme is illustrated in Fig. 3A and involves trapping with single quanta in cavity QED. Displayed is the energy-level diagram for the eigenstates of the coupled atom-cavity system (that is, the Jaynes-Cummings ladder of dressed states). We focus first on the spatial dependence of the energies

$\hbar\beta_\pm(\rho)$ for the first excited states $|\pm\rangle$ of the atom-cavity system along the radial direction $\rho = \sqrt{y^2 + z^2}$, for optimal standing-wave position x_0 [such that $\cos(2\pi x_0/\lambda) = 1$] and neglecting dissipation. The ground state of the atom-cavity system is $|a, 0\rangle$; the atom is in its ground state a and there are no photons in the cavity. For weak or no coupling, the first two excited states are that of one photon in the cavity and the atom in the ground state, $|a, 1\rangle$, and of the atom in the excited state e with no photons in the cavity, $|e, 0\rangle$. These two states are separated by an energy $\hbar\Delta_{ac}$, where $\Delta_{ac} \equiv \omega_{cavity} - \omega_{atom}$ is the detuning between the "bare" (uncoupled) atom and cavity resonances. As an atom enters the cavity along ρ, it encounters the spatially varying mode of the cavity field and hence a spatially varying interaction energy $\hbar g(\vec{r})$. The bare states map via this coupling to the dressed states $|\pm\rangle$ shown in Fig. 3A, with energies $\beta_\pm = (\omega_{atom} + \omega_{cavity})/2 \pm [g(\vec{r})^2 + (\Delta_{ac}^2/4)]^{1/2}$. Our interest is in the state $|-\rangle$. The spatial dependence of the energy $\hbar\beta_-(\vec{r})$ represents a pseudopotential well that can be selectively populated by our choice of the strength and frequency $\omega_{probe} = \omega_{atom} + \Delta_{probe}$ of an external driving field, thereby enabling an atom with kinetic energy $E_k \ll \hbar g_0$ to be trapped.

As discussed in more detail in the theory section below, Fig. 3B shows one example of the effective potential $U(\vec{r})$ that results from this trapping mechanism, which involves contributions from the higher lying levels shown in Fig. 3A, as well as the state $|-\rangle$. Displayed are both the radial and axial dependencies $U(\rho, x_0)$ and $U(0,x)$ (that is, perpendicular to and along the cavity axis, where x_0 is an antinode of the standing wave). The depth of the potential $U_0 \simeq 2.3$ mK is greater than the initial kinetic energy of atoms in our experiment, $E_k \simeq 0.46$ mK, thereby enabling an atom to be trapped within the cavity mode. The perturbing effect of gravity on this potential is negligible.

Also shown in Fig. 3B are the heating rates (mean rates of energy increase) $dE(\rho, x_0)/dt$ and $dE(0,x)/dt$ along the radial and axial directions, with dE/dt related to the momentum diffusion coefficient D by $dE/dt = D/m$, where m is the atomic mass of cesium. Near a field antinode (for example, $x = 0$), the random or diffusive component of the motion arising from dE/dt on experimental time scales of ~50 μs is on the whole much smaller than that associated with conservative motion in the potential U. Thus, we expect a predominantly orbital motion within the cavity mode with a smaller (but nonnegligible) diffusive component.

For comparison with the well-established theory of laser cooling and trapping in free space (*28*), Fig. 3B also displays in dashed lines the corresponding potential $V(\vec{r})$ and heating rate $d\mathscr{E}(\vec{r})/dt$ derived in the absence of the cavity, but for the same beam geometry and the same peak field strength (*29*). Al-

Fig. 2. (**A** and **B**) Examples of atom transits, that is, cavity transmission as a function of time as an atom passes through the cavity field. Red traces show atoms trapped with the triggering method described, with $\bar{m} \simeq 1$ photon mean field strength and with the dashed line at the level $\bar{n}_t$. For comparison, an untriggered (untrapped) atom transit is shown in black. For these traces, $\Delta_{probe}/2\pi = -125$ MHz and $\Delta_{ac}/2\pi = -47$ MHz. (**C** and **D**) Theoretical simulation of atom transits for the same Δ_{probe} and Δ_{ac}. Shot noise and technical noise were added to the transmission signals, shown in red. Other traces show the 3D motion of the atom. Motion along x, the standing-wave direction, was multiplied by 10 to be visible on the plot. The atom is very tightly confined in x until rapid heating in this direction causes the atom to escape.
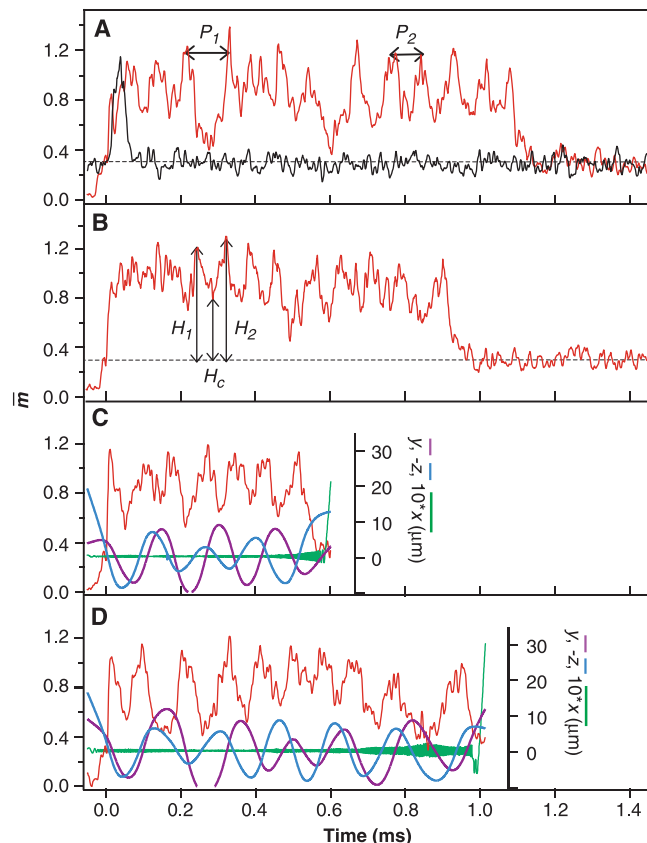
though the free-space potential $V(\vec{r})$ is similar to the cavity QED potential $U(\vec{r})$, suggesting that trapping could be achieved without the cavity [as, for example, in the pioneering experiments with optical lattices (30–32)], in fact, in the axial direction, the free-space heating rate $d\mathscr{E}/dt$ is much greater than the corresponding cavity QED quantity dE/dt. Indeed, the trapping time for an atom in the free-space setting would be more than 10-fold less than the observations of Fig. 2, so short that the atom would not even make one orbit before being heated out of the potential well.

We emphasize that the comparison in Fig. 3 is made for the same peak electric field—the cavity is not simply a convenient means for increasing the electric field for a given incident drive strength. Rather, there are profound differences between the standard theory of laser cooling and trapping and its extension into the domain of cavity QED in a regime of strong coupling. At root is the distinction between the nonlinear response of an atom in free space and one strongly coupled to an optical cavity. In the latter case, it is the composite response of the atom-cavity system illustrated in Fig. 3A that must be considered, as is described by the corresponding one-atom master equation in cavity QED. That this full quantum treatment of the atom-cavity system is required has been experimentally confirmed by way of measurements of the nonlinear susceptibility for the coupled system in a setting close to that used here (11–13).

A second and critically important point of distinction between the current work and traditional laser cooling and trapping in free space (28) relates to the ability to sense atomic motion in real time with high S/N ratios. We stress that this is not simply a matter of a practical advantage, but a fundamental improvement beyond what is possible by way of alternate detection strategies demonstrated to date [such as absorption (1, 2) or fluorescence (33–35) for single atoms and molecules]. An estimate of this enhanced capability is given by the ratio $R_c/R_0 \gg 1$, or alternatively by way of the optical information rate $I/\Delta t \sim 10^9/\mathrm{s}$, which in the current work is the largest value yet achieved in optical physics.

Apparatus and protocol. A cloud of cesium atoms was collected in a magneto-optical trap [MOT (28)], cooled to a temperature of $\simeq 20~\mu\mathrm{K}$ and then released, all in a vacuum chamber at 10^{-8} torr (Fig. 1). With initial mean velocity $\bar{v} \simeq 4$ cm/s, the cold atoms then fell 3 mm toward an optical resonator (cavity) (36) and reached velocity $v \simeq 24$ cm/s. Even with 10^4 atoms initially, only one or two atoms crossed the standing-wave mode of the cavity each time the MOT was dropped (37) (green arrows, Fig. 1).

We trapped an atom by driving the cavity with a weak circularly polarized probe laser at a frequency $\omega_{\mathrm{probe}} \simeq \beta_-(0)$ [corresponding to

$\beta(\vec{r})$ for maximum coupling, $g(\vec{r}) = g_0$] and intracavity photon number $\bar{n}_p = 0.05$ to provide small, off-resonant excitation of the empty cavity. With reasonable probability, a falling atom will be channeled by the resulting (shallow) potential $U_p(\vec{r})$ toward regions of high coupling, resulting in a corresponding increase in probe transmission as β_- comes into resonance with ω_{probe} in the fashion illustrated in Fig. 3A (11). When $g(\vec{r})$ exceeded some predetermined threshold g_t, we switched the probe power up to a level $\bar{n}_t = 0.3 \pm 0.05$ intracavity photons to create a deep confining potential $U(\vec{r})$ around the atom, thus trapping it (12). (We denote by $\bar{n}$ the photon number for the empty cavity and by $\bar{m}$ the corresponding quantity with an atom present; these quantities are directly proportional to the detected transmission signal.) The transmission was measured by heterodyne detection at 100-kHz bandwidth and digitized at 1 MHz, with an overall efficiency $\alpha = 25\%$ to detect an intracavity photon.

The probe transmission recorded by way of this protocol for two individual atom transits is displayed in Fig. 2, A and B. At time = 0, atom detection triggered the increase $\bar{n}_p \rightarrow \bar{n}_t$ to catch the atom. The cavity transmission was highest (with $\bar{m} \simeq 1$) when the atom was near the center of the cavity. The observed oscillations in $\bar{m}$ resulted from modifications in cavity transmission as the atom moved within the cavity mode. We emphasize that the corresponding quantum state is a bound state of atom and cavity. The situation is analogous to a molecule for which two atoms share an electron to form a bound state with a lower energy than two free atoms. Here a "molecule" of one atom and the cavity field is formed through the sharing of one photon excitation on average, thereby binding the

atomic CM motion. Our atom-cavity molecule only exists while an excitation is present, with decay set by κ, because $\kappa > \gamma$. To compensate for this decay-induced destruction of the atom-cavity molecule, the probe field continuously drove the cavity to repeatedly recreate the bound state before the atom had a chance to escape. When the atom eventually did leave the cavity mode, transmission returned to $\bar{n}_t$.

To demonstrate the strong effect of the triggering-trapping strategy, Fig. 2A also shows an atom transit (black trace) recorded with a drive strength of $\bar{n} = 0.3$ and no triggering. In this case, atoms fell through $U(\vec{r})$ with an average transit time of 74 μs. In contrast, the triggering protocol described above extended this average to 340 μs, in good agreement with theoretical simulations for both the mean and distribution of trap times. Indeed, many individual atom transits lasted much longer (the maximum observed time was 1.9 ms). Single atoms have recently been trapped with a lifetime of 28 ms in a regime of strong coupling by way of a classical dipole-force trap (15) but not with a quantum field at the single-photon level (38).

A striking feature of the traces in Fig. 2 are the oscillations in atom-cavity transmission. As illustrated in Fig. 2, C and D, our numerical simulations show that these oscillations arise from elliptical atomic orbits in planes perpendicular to the cavity axis. From the simulations discussed below, we find that motion along the cavity axis x is tightly confined to a region $\delta x \simeq \pm 50$ nm due to the steepness of $U(x)$ (39).

Theory and numerical simulations. Beyond the intuitive picture of trapping with the lower components of the dressed states as discussed in connection with Fig. 3, we car-
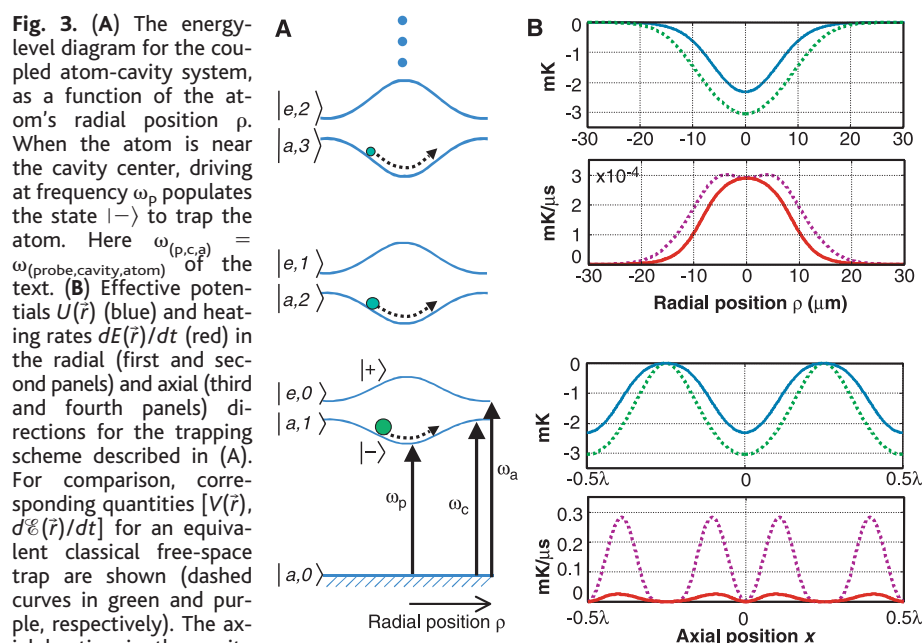
Fig. 3. (**A**) The energy-level diagram for the coupled atom-cavity system, as a function of the atom's radial position ρ. When the atom is near the cavity center, driving at frequency ω_p populates the state $|-\rangle$ to trap the atom. Here $\omega_{(p,c,a)} = \omega_{(\mathrm{probe,cavity,atom})}$ of the text. (**B**) Effective potentials $U(\vec{r})$ (blue) and heating rates $dE(\vec{r})/dt$ (red) in the radial (first and second panels) and axial (third and fourth panels) directions for the trapping scheme described in (A). For comparison, corresponding quantities [$V(\vec{r})$, $d\mathscr{E}(\vec{r})/dt$] for an equivalent classical free-space trap are shown (dashed curves in green and purple, respectively). The axial heating in the cavity trap is 10-fold smaller, greatly enhancing the trap lifetime. All quantities are calculated for $\Delta_{\mathrm{probe}}/2\pi = -145$ MHz and $\Delta_{\mathrm{ac}}/2\pi = -74$ MHz, with empty cavity photon number $\bar{n} = 0.3$.

ried out extensive analytical and numerical simulations of atomic motion for the parameters of our experiment, following the basic model of (23). As is the case for motion of an atom in a free-space standing wave (40, 41), there is a separation of time scales between the internal (atomic dipole + cavity field) degrees of freedom and the external atomic CM motion. The effective potential $U(\vec{r})$ presented in Fig. 3 is determined by integration of the expectation value of the force operator:

$$\hat{\mathbf{F}}(\vec{r}) = -\hbar\nabla g(\vec{r})(\hat{a}^{\dagger}\hat{\sigma}_{-} + \hat{\sigma}_{+}\hat{a}) \quad (1)$$

with $(\hat{a}, \hat{a}^{\dagger})$ as the annihilation and creation operators for photons in the cavity field and $\hat{\sigma}_{\pm}$ as the raising and lowering operators for atomic excitation. There are also nonconservative (velocity-dependent) and random (diffusive) forces that act on the atom and are described by matrices $\alpha(\vec{r})$ and $\mathcal{D}(\vec{r})$, respectively. The nonconservative forces may include cooling such as the Sisyphus cooling mechanism discussed in (24). The diffusive forces have a component due to "recoil kicks" from spontaneous emission that is the dominant contribution for the radial motion and a reactive component due to fluctuations of the atomic dipole that is substantial for motion along the direction of the optical standing wave. All of the contributions to the atomic CM motion are strongly position dependent. For example, the reactive component of $\mathcal{D}(\vec{r})$ depends on the square of the gradient of the coupling $g(\vec{r})$ as well as the atomic internal state at $\vec{r}$, so that this contribution to $\mathcal{D}(\vec{r})$ is strongly suppressed around the antinodes of the standing wave. The separation of time scales in the problem means that all of the quantities $\{U(\vec{r}), \alpha(\vec{r}), \mathcal{D}(\vec{r})\}$ may be evaluated by solving the steady-state quantum master equation for the internal degrees of freedom alone (42, 43). Hence, the local atom-field coupling $g(\vec{r})$, probe

parameters ($\mathcal{E}_{probe}$, Δ_{probe}), and detuning Δ_{ac} suffice to determine the various forces on the atom at $\vec{r}$.

The motion of an atom in the cavity may be simulated by means of a system of Langevin equations for the position and momentum $\vec{p}$ of the atom:

$$\frac{d}{dt}\vec{r} = \frac{\vec{p}}{m} \quad (2)$$

$$\frac{d}{dt}\vec{p} = \langle\hat{\mathbf{F}}(\vec{r})\rangle - \alpha(\vec{r})\frac{\vec{p}}{m} + B(\vec{r})\vec{e}(t) \quad (3)$$

where B is such that $\mathcal{D}(\vec{r}) = B(\vec{r})B^{T}(\vec{r})/2$ and the vector $\vec{e}(t)$ is made up of noises of zero mean that are delta-correlated in time (44). These equations allow us to investigate the statistics of the length of time atoms spend in the cavity and the characteristics of atomic oscillation in the optical potential as discussed below, as well as the characteristics of the heating processes. The ensemble of these trajectories provides information about the correlation between the motional dynamics and the cavity field state (38), which in turn forms the basis of the reconstruction algorithm for the atomic motion discussed below. In the experimental regime, spontaneous emission will lead to a coherence length of the quantum mechanical state of motion that is small compared with the length scales of the variation of the coupling $g(\vec{r})$, and as a result, individual trajectories of such simulations may be tentatively identified with the random motion of the mean position and momentum of a localized atomic wave packet.

The simulations as well as observations (39) indicate that the motion along the cavity axis x is tightly confined (for example, to a region $\delta x \simeq \pm 50$ nm from the simulations) because of the steepness of $U(x)$. However, as shown in

Fig. 2, C and D, ultimately the atom does escape because of a "burst" of heating along the cavity axis that occurs over a time less than the orbital period. This dominant loss mechanism appears repeatedly in the simulations over a wide range of operating parameters. The mechanism for this heating is the very steep growth of the diffusion constant away from the antinode. Once an atom is heated sufficiently to leave the antinode to which it was initially confined, it is very rarely recaptured in another antinode but rather escapes the cavity altogether, because the Sisyphus-type mechanisms (24) for cooling are ineffective in the current setting (as confirmed in our simulations).

Validation of $U(\rho)$. Restricting our attention then to motion in transverse $(y, z) \rightarrow (\rho, \theta)$ planes, we can investigate the validity of our model for the effective potential $U(\rho)$ by comparing the predicted and observed oscillation frequencies. Oscillations with a short period (P_2 in Fig. 2A) have a smaller amplitude than those of longer period (P_1 in Fig. 2A) because of the anharmonicity of our approximately Gaussian-shaped potential $U(\rho)$; large-amplitude oscillations are expected to have a longer period than nearly harmonic oscillations at the bottom of the well. The data in Fig. 4A reveal this anharmonicity. Plotted is the period P versus the amplitude A for individual oscillations, where $A \equiv 2[(H_1 + H_2)/2 - H_c]/(H_1 + H_2)$, with parameters $\{H_1, H_2, H_c\}$ indicated in Fig. 2B. The blue curve is calculated for motion in the effective potential $U(\rho)$ shown in the inset to Fig. 4A; the comparison is absolute with no adjustable parameters.

We also present in Fig. 4B similar results for A versus P from our numerical simulations (for the same parameters as Fig. 4A). This plot reveals the relative importance of different mechanisms that cause deviations from the one-dimensional (1D), conservative-force model. To this end, we select from the simulation points corresponding to atoms with low angular momentum about the center of the cavity, that is, those that pass close to the center of the potential ($\rho = 0$) and therefore have close to a 1D trajectory. As expected, these points (shown in blue in Fig. 4B) fall closest to the curve given by the 1D potential $U(\rho)$. The green points in Fig. 4B have larger angular momentum, corresponding to atoms in more circular orbits. The presence of this separation by angular momentum in the simulation indicates that friction and momentum diffusion, which tend to invalidate the conservative-force model, have a relatively small effect on the motion, as is evident from the plots of $U(\vec{r})$ and $dE(\vec{r})/dt$ in Fig. 3B. The spread in observed angular momenta is constrained by our triggering conditions—the potential is switched up only when an atom reaches a position near the center of the cavity mode, so that the measured trajectories tend to be in a regime of tight binding. The wider spread in the data of Fig. 4A relative to Fig. 4B comes from

Fig. 4. Oscillation period as a function of amplitude from (**A**) experimental and (**B**) simulated atom transits, for the parameters of Fig. 3B. Calculated 1D oscillation in the anharmonic effective potential (inset) is shown by the blue curve, with no adjustable parameters. In simulated data, note the separation of data points by angular momentum; lowest angular momentum transits (blue) most closely follow the 1D model.
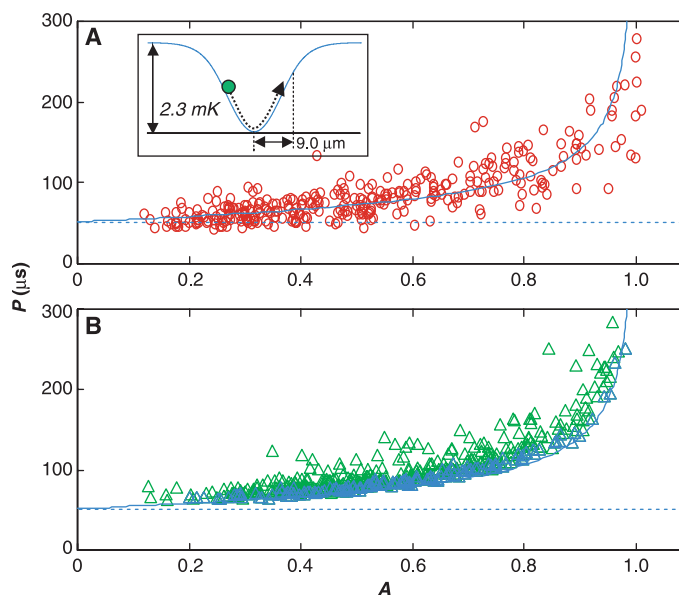
experimental noise (present in Fig. 4A but not added to Fig. 4B), with both shot noise and technical noise contributing substantially. We made comparisons as in Fig. 4 for several data sets with varying values of $\{(\mathscr{E}_{probe}, \Delta_{probe}), \Delta_{ac}, \bar{n}_t\}$ with the same conclusions.

Reconstruction of atomic orbits. Our understanding of atomic motion in the effective potential $U(\rho)$ (including confirmation that motion in the standing-wave direction is minimal) together with a knowledge of the mapping between atom position and probe beam transmission via the master equation enables accurate reconstructions of 2D trajectories for the individual atom transits of Fig. 2. The reconstruction algorithm consists first of digitally filtering the transmission data of Fig. 2 with a 20-kHz low-pass Butterworth filter to reduce noise unrelated to the atomic motion. The smoothed transmission is then mapped to atomic radial position to obtain $\rho(t)$. To infer a 2D trajectory for the atom, it is necessary to determine $\theta(t)$ as well. If we consider that the atom orbits in a known central potential, the solution to this problem becomes apparent. The angular momentum of such an orbit can be calculated from the maximum and minimum radius it attains, via

$$L = \rho_{max}\rho_{min}\sqrt{\frac{2m[U(\rho_{max}) - U(\rho_{min})]}{(\rho_{max}^2 - \rho_{min}^2)}}$$

(4)

where m is the atomic mass. An atom in our cavity does not orbit in a strictly conservative potential, so its angular momentum and orbit change over time because of the velocity-dependent and random forces discussed above. However, if the angular momentum changes by a small fractional amount in the course of a single orbit, we may use successive maximum and minimum radial positions $\rho_{max}^i, \rho_{min}^i$ to estimate a piecewise angular momentum L^i for each half-orbital period. A smooth interpolation in L can then be made along the segments from L^i to L^{i+1}. Knowledge of $\rho(t)$ and $L(t)$ allows determination of $\theta(t)$ via $\dot{\theta} = L/m\rho^2$. We stress that trajectories derived from this algorithm contain three fundamental ambiguities: the initial angle of entry, the overall sign of the angular momentum, and the specific antinode in which the orbit is confined. These initial conditions are not given by the reconstruction algorithm and may be considered degrees of freedom in the final result. In the trajectories of Fig. 5, A and B, the initial angle was chosen to display the atoms falling into the cavity from above, as is physically appropriate. In Fig. 5, C and D, the initial conditions were chosen to provide best agreement with the corresponding actual (simulated) trajectories.

We validated this inversion algorithm by analyzing a series of the simulated atom transits and associated transmissions (as in Fig. 2, C and D). Atomic trajectories are reconstructed from the simulated transmission (including fundamental and technical noise) via our algorithm

and compared with the actual positions from the simulation. Particular results for the simulations of Fig. 2, C and D, are shown in Fig. 5, C and D, respectively, where the actual trajectory is traced in gray, with the reconstruction in green. The quality of these reconstructions is typical of the results for most atom trajectories. In general, reconstructions exhibit good agreement until the very end of the trajectory, where our algorithm fails because (i) the angular momentum cannot be estimated once the atom has escaped from a bound orbit and (ii) the reconstruction ignores x axis motion, which becomes nonnegligible at the end of the trajectory (see Fig. 2, C and D).

For a small fraction of atom transits, our reconstruction method cannot be applied reliably. These are the atoms with nearly linear orbits that pass near the origin of the potential. Reconstructions fail in this case because these atoms have very low angular momentum that changes by a large fraction in the course of a single orbit and may even change sign from one orbit to the next. Such cases are characterized by distinct oscillations in the cavity transmission that repeatedly reach the maximum allowed value of $\bar{m}$ for the known probe parameters ($\mathscr{E}_{probe}, \Delta_{probe}$) and detuning Δ_{ac}. Reconstructions were not attempted in such cases and,

indeed, when attempted tended to produce reconstructed trajectories with sharp corners and unphysical kinks near the origin (*45*).

On the basis of this ability to reconstruct trajectories in the simulations (with the associated caveats), we applied the same technique to the actual experimental data. In this way, the two individual atom transits of Fig. 2, A and B, were translated into the trajectories of Fig. 5, A and B, respectively. We now see directly that the transmission changes of Fig. 2, A and B, relate to elongated orbits, with time-varying distance to the cavity center. The size of the green dot at the start of each trajectory indicates the typical error in the estimate of the atomic location, from comparisons as in Fig. 5, C and D (*46*).

Extensions of the ACM. Subject to the caveats concerning the reconstruction algorithm, the results of Fig. 5 represent a capability for tracking the position of a single atom with about 2-μm resolution achieved on a 10-μs time scale. Stated in terms of a sensitivity S_ρ for tracking atomic motion in the radial plane, these numbers translate to $S_\rho \simeq 2 \times 10^{-8}$ m/$\sqrt{\text{Hz}}$, as set by (among other things) the slope of the cavity mode in the radial direction, $|d\psi(\vec{r})/d\rho|_{max} \sim w_0^{-1}$. Increasing this slope would lead directly into

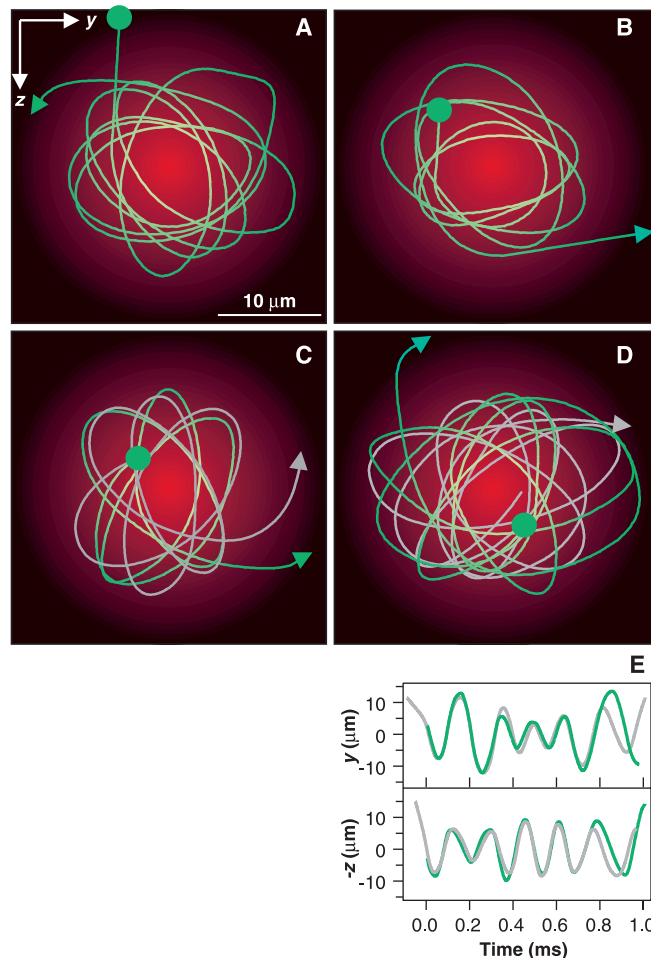**Fig. 5.** Atom trajectories lie in a plane perpendicular to the cavity axis, as illustrated by the schematic in Fig. 1. (**A** and **B**) Reconstructed atomic trajectories for the transits of Fig. 2, A and B. (**C** and **D**) Trajectories reconstructed from the simulated transits of Fig. 2, C and D, with the actual trajectories shown in gray for comparison. (**E**) Positions $y(t)$ and $z(t)$ for (D) are shown for clarification. The green dot at the start of each reconstructed trajectory indicates an estimated error in the reconstruction. Animated versions of these orbits can be viewed at www.its.caltech.edu/~qoptics/atomorbits/.

improvements in sensitivity, both through the explicit increase in the rate of change of the coupling coefficient with displacement $dg(\vec{r})/d\rho$ as well as through the implicit increase in g_0 with reduced cavity volume V_C [and hence also decreases in the critical parameters (n_0, N_0)].

Although the axial motion was not observed in our current experiments, we can nonetheless make an estimate of the sensitivity S_x for detecting atomic position along the standing wave direction through the simple relation $|d\psi/dx|_{max}/|d\psi/d\rho|_{max} \sim 10^2$, leading to $S_x \simeq 2 \times 10^{-10}$ m/$\sqrt{Hz}$. This estimate should be compared with that of (13), namely $S_x \simeq 1 \times 10^{-10}$ m/$\sqrt{Hz}$, which was, however, obtained by operating in a dispersive regime and detecting the full optical phase to optimize sensitivity. Given that there is a large separation in time scales associated with motion in the radial and axial dimensions $(\sim |d\psi/d\rho|_{max}/|d\psi/dx|_{max})$, a possible strategy for full 3D reconstruction of atomic motion within the cavity would be to split the detected photocurrent into two components—one with a low-pass filter relating to the radial motion and another with a high-pass filter for the axial motion. Additionally, ambiguities in the initial angle and the sign of the angular momentum may in principle be overcome by strategies that break the radial symmetry, such as the use of external field gradients or transverse cavity modes.

With respect to fundamental quantum limits of the ACM, we estimate that the sensitivity S_ρ together with the time of our observations brings us close to the standard quantum limit (SQL) for position measurement. The SQL is the limit at which measurement-induced back action on the momentum of the particle becomes an important component in the noise budget for position sensing and can limit further improvements in sensitivity (47). Initial estimates based on the theoretical analysis of (48) indicate that the current experiment is perhaps a factor of five above the SQL, which is again consistent with the estimate of (13). Straightforward improvements to the experiment [such as enhanced detector quantum efficiency, a single-sided versus the current two-sided cavity, and reduced technical noise along the lines of (13)] should improve both the spatial and temporal resolution of our ACM for monitoring atomic motion.

Implicit in this ability to sense with high sensitivity and bandwidth is the possibility for control of a single atomic trajectory by quantum feedback. By implementing our inversion algorithm in real time, a suitable error signal can be derived to modulate the effective potential $U(\vec{r}) \rightarrow U(\vec{r}, t)$ in a fashion that damps atomic motion to the bottom of the well. Indeed, with generalized strategies for active control, it should be possible to surpass the SQL and to synthesize novel nonclassical states of motion (49).

Even without reaching such fundamental limits and extremely low levels of incident light ($\bar{m} \lesssim 1$ photon in the cavity), we suggest that the type of real-time microscopy represented by the ACM might be more broadly applicable to monitoring of chemical and biological processes at the single-molecule scale. In this setting, a key feature of the ACM would be the ability to sense changes of the optical properties of an intracavity medium with high bandwidth and sensitivity. The function of localization within the cavity mode would be provided by a separate means other than the single-photon trapping used in the current work (as, for example, by an optical dipole-force trap or indeed by in vitro diffusion).

Certainly optical techniques already exist with single-molecule resolution (34, 35, 50–53). However, a potentially powerful aspect of the ACM would be the ability to track molecular dynamics in real time for a single molecule within a resolution volume within the cavity. Implicit in realizing such a capability would be a detailed understanding of the nature of the radiative interaction between molecule and cavity field, as well as of the detection mechanism, thereby allowing the development of an inversion algorithm such as that leading to the results of Fig. 5, where now the "trajectory" could be in a space such as, for example, molecular conformations (54).

Although it might seem at first sight hopeless to accomplish this for complex chemical or biological species, in fact, the situation can be considerably simpler than in the full quantum case presented here. In many situations, knowledge only of the linear susceptibility of the particle in question should be sufficient for the purpose of realizing an ACM. A rather extensive theory of the input-output characteristics for cavities containing such linear (or indeed nonlinear) media exists within the context of the literature on optical bistability (55). Within this setting, the key parameters become the so-called cooperativity parameter C_1 for a single particle ($\sim 1/N_0$ for our experiment) and the saturation intensity I_s for the intracavity field [$\sim n_0 c/(\hbar \omega V_C)$], both of which can be determined by traditional means with bulk samples. Of particular interest might be detection of dispersive shifts of the cavity resonance by a target molecule, thereby potentially avoiding photobleaching. What is required is an extension of this literature directed toward the development of suitable inversion algorithms, as has been carried out in one particular case in this research article.

An alternative to such a case-specific approach involving the direct modification of the cavity field by an intracavity molecule is to exploit a detailed knowledge of the atom-cavity interaction to sense molecular dynamics indirectly. Consider an atom (e.g., cesium as here) trapped within the cavity mode but subject to an additional interaction with a molecule that has negligibly small direct coupling to the cavity field. The interaction energy of the (sensing) cavity atom and (sensed) molecule leads to changes in the level structure of the cavity atom as well as to a force that shifts the equilibrium atomic position within the cavity. In either event, the amplitude and phase of the transmitted field are modified, from which an inference of the molecular interaction (such as dipole-dipole coupling) can be drawn. We envision a geometry that would allow the atom-cavity system to be scanned spatially, thereby combining the very high quality factors available from the atom-cavity interaction with more conventional scanning probe microscopies.

References and Notes

1. D. J. Wineland, W. M. Itano, J. C. Bergquist, *Opt. Lett.* **12**, 389 (1987).
2. W. E. Moerner and L. Kador, *Phys. Rev. Lett.* **62**, 2535 (1989).
3. The finesse is assumed to be large compared with the cavity Fresnel number to ensure rapid diffractive mixing within the cavity lifetime.
4. For a discussion, see L. A. Orozco *et al.*, *Phys. Rev.* **39**, 1235 (1989).
5. G. Rempe, R. J. Thompson, H. J. Kimble, R. Lalezari, *Opt. Lett.* **17**, 363 (1992).
6. G. Rempe, *Appl. Phys. B* **60**, 233 (1995).
7. P. Cerez, A. Brillet, C. N. Man-Pichot, R. Felder, *IEEE Trans. Instrum. Meas.* **29**, 352 (1980).
8. M. de Labachlelerie, K. Nakagawa, M. Ohtsu, *Opt. Lett.* **19**, 840 (1994).
9. J. Ye, L.-S. Ma, J. L. Hall, *Opt. Lett.* **21**, 1000 (1996).
10. H. Mabuchi, Q. A. Turchette, M. S. Chapman, H. J. Kimble, *Opt. Lett.* **21**, 1393 (1996).
11. C. J. Hood, M. S. Chapman, T. W. Lynn, H. J. Kimble, *Phys. Rev. Lett.* **80**, 4157 (1998).
12. J. Ye *et al.*, *IEEE Trans. Instrum. Meas.* **48**, 608 (1999).
13. H. Mabuchi, J. Ye, H. J. Kimble, *Appl. Phys. B* **68**, 1095 (1999).
14. P. Münstermann *et al.*, *Phys. Rev. Lett.* **82**, 3791 (1999).
15. J. Ye, D. W. Vernooy, H. J. Kimble, *Phys. Rev. Lett.* **83**, 4987 (1999).
16. P. Berman, Ed., *Cavity Quantum Electrodynamics* (Academic Press, San Diego, CA 1994).
17. For a more recent review, see contributions in the Special Issue of *Physica Scripta* **T76**, (1998).
18. G. Rempe, F. Schmidt-Kaler, H. Walther, *Phys. Rev. Lett.* **64**, 2783 (1990).
19. G. Rempe, R. J. Thompson, R. J. Brecha, W. D. Lee, H. J. Kimble, *Phys. Rev. Lett.* **67**, 1727 (1991).
20. M. Brune *et al.*, *Phys. Rev. Lett.* **77**, 4887 (1996).
21. S. Haroche, M. Brune, J. M. Raimond, *Europhys. Lett.* **14**, 19 (1991).
22. B. G. Englert, J. Schwinger, A. O. Barut, M. O. Scully, *Europhys. Lett.* **14**, 25 (1991).
23. A. C. Doherty, A. S. Parkins, S. M. Tan, D. F. Walls, *Phys. Rev. A* **56**, 833 (1997).
24. P. Horak *et al.*, *Phys. Rev. Lett.* **79**, 4974 (1997).
25. M. O. Scully *et al.*, *Phys. Rev. Lett.* **76**, 4144 (1996).
26. W. Ren and H. J. Carmichael, *Phys. Rev. A* **51**, 752 (1995).
27. D. W. Vernooy and H. J. Kimble, *Phys. Rev. A* **56**, 4287 (1997).
28. For an overview of atom trapping techniques, see the Nobel Lectures by S. Chu [*Rev. Mod. Phys.* **70**, 685 (1998)], C. Cohen-Tannoudji [*Rev. Mod. Phys.* **70**, 707 (1998)], and W. D. Phillips [*Rev. Mod. Phys.* **70**, 721 (1998)].
29. C. Cohen-Tannoudji, in *Fundamental Systems in Quantum Optics, Les Houches, Session LIII, 1990*, J. Dalibard, J. M. Raimond, J. Zinn-Justin, Eds. (Elsevier Science, Amsterdam, 1992), pp. 21–52.
30. P. Verkerk *et al.*, *Phys. Rev. Lett.* **68**, 3861 (1992).
31. P. S. Jessen *et al.*, *Phys. Rev. Lett.* **69**, 49 (1992).
32. P. Marte, R. Dum, R. Taieb, P. D. Lett, P. Zoller, *Phys. Rev. Lett.* **71**, 1335 (1993).
33. R. J. Cook, in *Progress in Optics*, vol. XXVIII, E. Wolf, Ed. (North Holland, Amsterdam, 1990), p. 361.

34. M. Oritz, J. Bernard, R. Personov, *Phys. Rev. Lett.* **65**, 2716 (1990).
35. W. P Ambrose and W. E. Moerner, *Nature* **349**, 225 (1991).
36. The optical cavity is formed by two 1-mm diameter, 10-cm radius of curvature mirrors, located on the tapered end of 4 mm by 3 mm glass substrates. The multilayer dielectric mirror coatings have a transmission of 4.5×10^{-6} and absorption/scatter losses of 2.0×10^{-6}, giving rise to a cavity finesse $F = 480,000$. For the measured cavity length $l = 10.9 \, \mu m$ and waist $w_0 = 14 \, \mu m$, we have parameters $(g_0, \kappa, \gamma) = 2\pi(110, 14.2, 2.6)$ MHz, where these rates refer to the transition $\{|a\rangle \equiv 6S_{1/2}, F = 4, m_F = 4\} \rightarrow \{|e\rangle \equiv 6P_{3/2}, F = 5, m_F = 5\}$ at $\lambda = 852$ nm in atomic cesium.
37. To interact with light in the cavity mode, an atom must fall through the 9-μm gap between the edges of the mirrors and also through the waist $w_0 = 14 \, \mu$m of the Gaussian mode of the resonator.
38. Our numerical simulations indicate that the intracavity field exhibits manifestly quantum or nonclassical characteristics for the parameters used in the experiment. For example, the normalized two-time intensity correlation function $\simeq 0.9$ for short time delays, where a value < 1 indicates nonclassicality.
39. Experimentally, we can set a limit on atomic excursions along x by examining the amplitude of the observed oscillations. Because the oscillation frequency $\nu_x \simeq 1.5$ MHz is well above our detection bandwidth of 100 kHz, large excursions in x would lead to substantial reduc-

tions in amplitude for the observed oscillations in transmission, from which we deduce a bound $\delta x^e \lesssim 70$ nm for $\rho \ll w_0$. Inference of axial localization without such bandwidth limitations can be found in (*13*).
40. J. Dalibard and C. Cohen-Tannoudji, *J. Phys. B* **18**, 1661 (1985).
41. J. P. Gordon and A. Ashkin, *Phys. Rev. A* **21**, 1606 (1980).
42. The approximations used in some of the calculations of (*23*) and also the weak driving approximation of (*24*) are not appropriate in the regime of the current work. All quantities are calculated numerically from the full quantum master equation for the internal degrees of freedom.
43. This part of the calculation was performed with a code based on Sze Tan's "Quantum Optics Toolbox," available at www.phy.auckland.ac.nz/Staff/smt/qotoolbox/download.html
44. These are technically stochastic differential equations written in their Ito form.
45. On first inspection, it might seem that the reconstruction algorithm should fail for circular orbits as well, because in the absence of large transmission oscillations the algorithm will rely on small differences between ρ^i_{max} and ρ^i_{min}, which are uncertain because of technical and detection noise. However, the resulting estimated angular momentum closely approximates that of a circular orbit at radius $\rho^i_{max} \simeq \rho^i_{min}$ and is therefore the correct angular momentum for the orbit.
46. A more extensive gallery of reconstructed orbits can be

viewed at www.its.caltech.edu/~qoptics/atomorbits/gallery.html.
47. V. B. Braginsky and F. Ya. Khalili, *Quantum Measurement* (Cambridge Univ. Press, Cambridge, 1992).
48. H. Mabuchi, *Phys. Rev. A* **58**, 123 (1998).
49. J. A. Dunningham, H. M. Wiseman, D. F. Walls, *Phys. Rev. A* **55**, 1398 (1997).
50. E. Betzig and R. J. Chichester, *Science* **262**, 1422 (1993).
51. X. S. Xie and J. K. Trautman, *Annu. Rev. Phys. Chem.* **49**, 441 (1998).
52. W. E. Moerner and M. Orrit, *Science* **283**, 1670 (1999).
53. S. Weiss, *Science* **283**, 1676 (1999).
54. H. Mabuchi *et al.*, in preparation.
55. H. M. Gibbs, *Optical Bistability: Controlling Light with Light* (Academic Press, Orlando, FL, 1995).
56. We gratefully acknowledge the contributions of K. Birnbaum, M. S. Chapman, H. Mabuchi, J. Ye, and S. Tan to the current research. This work is supported by the NSF, by the Office of Naval Research, by the Defense Advanced Research Projects Agency via the Quantum Information and Computation Institute administered by Army Research Office, and by Hewlett-Packard Research Labs. Work at the University of Auckland is supported by the Marsden Fund of the Royal Society of New Zealand.

An Oral Vaccine Against NMDAR1 with Efficacy in Experimental Stroke and Epilepsy

Matthew J. During,[1,3]* **Charles W. Symes,**[1] **Patricia A. Lawlor,**[1] **John Lin,**[2] **Jane Dunning,**[1] **Helen L. Fitzsimons,**[1] **David Poulsen,**[3] **Paola Leone,**[3] **Ruian Xu,**[1] **Bridget L. Dicker,**[1] **Janusz Lipski,**[2] **Deborah Young**[1]

The brain is generally considered immunoprivileged, although increasing examples of immunological responses to brain antigens, neuronal expression of major histocompatibility class I genes, and neurological autoimmunity have been recognized. An adeno-associated virus (AAV) vaccine generated autoantibodies that targeted a specific brain protein, the NR1 subunit of the *N*-methyl-D-aspartate (NMDA) receptor. After peroral administration of the AAV vaccine, transgene expression persisted for at least 5 months and was associated with a robust humoral response in the absence of a significant cell-mediated response. This single-dose vaccine was associated with strong anti-epileptic and neuroprotective activity in rats for both a kainate-induced seizure model and also a middle cerebral artery occlusion stroke model at 1 to 5 months following vaccination. Thus, a vaccination strategy targeting brain proteins is feasible and may have therapeutic potential for neurological disorders.

In the central nervous system (CNS), both the NMDA and non-NMDA subclasses of glutamate receptors are mediators of glutamatergic

[1]Department of Molecular Medicine and [2]Department of Physiology, University of Auckland School of Medicine, Auckland, New Zealand. [3]Department of Neurosurgery, Jefferson Medical College and Thomas Jefferson University, Philadelphia, PA 19107, USA.

*To whom correspondence should be addressed. E-mail: matthew.during@mail.tju.edu

excitatory neurotransmission. NMDA receptors are of major interest, as they are involved in many processes necessary for brain development including neuronal migration (*1*), patterning of afferent termination (*2*), and several forms of long-term synaptic plasticity (*3*). Properties of the receptor include calcium permeability, voltage-dependent Mg^{2+} block, and slow channel kinetics (*4*). Molecular cloning has revealed three receptor subunit families (NR1, NR2, and NR3A) which form

hetero-oligomeric complexes in native NMDA receptor channels (*5, 6*). NR1 subunits are essential for the formation of functional NMDA receptors, whereas addition of other subunits modifies receptor properties (*6, 7*). In addition to the role of NMDA receptors in brain plasticity and development, they have also been implicated as a mediator of neuronal injury associated with many neurological disorders including stroke, epilepsy, brain trauma, dementia, and neurodegenerative disorders (*8*).

Because of their central involvement in the cascade leading to neuronal death following a variety of cerebral insults, pharmacological NMDA receptor antagonists have been evaluated for potential clinical use. These drugs are effective in many experimental animal models of disease, and some of these compounds have moved into clinical trials (*9*). However, the initial enthusiasm for this approach has waned, because the therapeutic ratio for most NMDA antagonists is poor, with significant adverse effects at clinically effective doses, thus limiting their utility (*9*).

As an alternative approach to antagonize NMDA receptors, we investigated the hypothesis that a humoral autoimmune response targeting the NR1 subunit of NMDA receptor might have neuroprotective activity. Moreover, we also hypothesized that such autoantibodies would have minimal penetration into the CNS under basal conditions and thereby avoid the toxicity associated with traditional approaches, but following a cerebral insult, would pass into the brain more efficiently, antagonize the receptor, and thereby attenuate NMDA receptor–mediated injury.

Oral genetic vaccination with recombinant AAV. We used an oral genetic vaccine

The Atom-Cavity Microscope: Single Atoms Bound in Orbit by Single Photons

C. J. Hood *et al.*

Science **287**, 1447 (2000);
DOI: 10.1126/science.287.5457.1447